Development and Characterization of a pH-Independent, Plasticizer-Free, Ionophore-Based Sodium Nanosensor for Use in *In Vivo* Photoacoustic Medical Imaging

By Jacalyn H. Wasserman

Honors Biophysics Senior Thesis
Kopelman Lab
University of Michigan
12/19/2022

Abstract

Measuring sodium (Na^+) concentration has widespread applications ranging from water quality testing to medical diagnostics. Nanosensors are uniquely well-suited to *in vivo* chemical imaging applications because they are minimally invasive, capable of providing 3D spatial resolution, and can be functionalized to target specific tissues or cells. However, such applications require a non-toxic nanosensor that has both high sensitivity to and selectivity for Na^+ in physiological conditions. To the author's knowledge, there are no previously reported sodium nanosensors in the literature that meet all of these criteria, primarily due to low sensitivities across physiological Na^+ concentrations, reliance on pH-dependent dyes, or toxicity concerns. Herein, a plasticizer-free, ionophore-based sodium nanosensor, SD NaNP, was developed and characterized with a focus on applications in photoacoustic cancer imaging. SD NaNP is sensitive to physiologically relevant Na^+ concentrations and produces a strong ratiometric response of 520 nm over 630 nm spectral absorbance. Moreover, as detailed in this paper, SD NaNP is non-toxic, is highly insensitive to pH and other analytes, is 23.42 nm in radius when filtered, and was successfully applied to *in vitro* photoacoustic calibrations.

Table of Contents

I. Introduction

The sodium ion (Na^{+}) is an important biological analyte whose varied roles include those in action potential generation, nutrient transport, osmotic control, inflammation, and blood volume regulation[1,2]. Accordingly, sodium sensing has numerous biological applications, especially for the study and monitoring of diseases in which these Na^{+}-mediated processes are disrupted[2]. In particular, recent interest has been generated in measuring sodium concentrations of the tumor microenvironment (TME) because changes in sodium homeostasis have been correlated to increased tumor growth, metastasis, invasion, and immune cell inhibition[1,3]. However, while much effort has been devoted to *in vitro* sodium sensing, the adaptation of these principles to *in vivo* applications, such as cancer imaging, remains a challenge[1]. The primary reasons for this difficulty are issues regarding sensor toxicity, invasiveness, detection limits, cross-sensitivity to other analytes, and light scattering by biological tissues[1,4].

Nanosensors offer a promising method of overcoming several of these barriers because they are suitable for *in vivo* administration, localize to tumors, are minimally invasive, and provide 3D spatial resolution[5]. However, current sodium nanosensing technology does not meet all of the criteria of *in vivo* imaging applications. The primary drawbacks of previously reported sodium nanosensors[2,4,6-11] include toxicity concerns, cross sensitivity to pH or other cations, suboptimal sensitivity to Na^{+} over physiological concentration ranges, or large particle sizes that inhibit effective diffusion to the tumor site. Furthermore, many fluorescence-based sodium nanosensors, which represent a major class of nanosensors[5], use single wavelength fluorescence measurements[2,4,10-11] that require precise control of sensor concentration which is difficult to achieve *in vivo*[8]. Comparatively, ratiometric responses, such as that reported herein, are better suited to situations in which sensor concentration may vary[8]. Most fluorescence-based

nanosensors[2,4,9,11] also absorb or fluoresce at wavelengths below 500 nm, which significantly limits their penetration depth due to light scattering by biological tissues[4,12]. As is commonly used for medical imaging and has been applied by the Kopelman Lab to oxygen and pH nanosensing systems, one method of extending penetration is to use photoacoustic imaging (PAI)[12-13]. In PAI, a red or infrared laser pulse (typically, 550 – 900 nm[13]) is selectively absorbed by nanosensors in the tumor, causing thermal excitation that produces detectable ultrasound waves[12-14]. By combining optical imaging and ultrasound, PAI enables deeper tissue imaging (up to a few centimeters[13]) than light alone would while being sensitive to chemical concentrations in a way that could not be accomplished by ultrasound alone[13].

Therefore, the goal of this research project was to make a sodium nanosensor that could be applied to *in vivo* photoacoustic chemical imaging of the TME. To this end, an ionophore-based sodium nanosensor, SD NaNP, was developed and characterized. Similar to other ionophore-based nanosensors[5], this sodium sensor consists of (1) an ionophore to bind the analyte of interest, (2) a dye whose absorption reports on the analyte concentration, (3) a counterion for charge balance, and (4) a polymer capsule. A solvatochromic dye, whose absorption depends on the hydrophobicity of its environment, was used instead of a protonatable dye to eliminate cross-sensitivity to pH. Additionally, the dye exhibits a ratiometric absorbance response of 520 nm over 630 nm spectral absorbance. In contrast to most nanosensors, SD NaNP is plasticizer-free, reducing toxicity and material cost. Upon characterization, the SD NaNP nanosensor was shown to be (1) sensitive to physiologically relevant Na^+ concentrations, (2) pH-independent, (3) selective against non-sodium cations, and (4) biocompatible.

II.   Background

1. Role of Sodium in the Tumor Microenvironment

The tumor microenvironment (TME) refers to the chemically unique milieu of endogenous compounds and structures that surround cancer cells[15-16]. Hallmark characteristics of the TME, such as hypoxia and increased acidity, differentiate it from healthy tissue[15-16]. Moreover, the composition of the TME has been well-established to influence tumor growth, metastasis, and treatment response. For example, increased K^+ concentrations have been linked to immune cell evasion and associated poor response to immunotherapy[12]. As such, extensive research efforts have been devoted to characterizing the TME to identify potential biomarkers of cancer.

One such biomarker present in the TME is the sodium ion. The correlation between high sodium concentrations and cancer has been documented in the literature since the 1980s[3]. Early studies noted elevated salt concentrations in breast cancer tumors compared to healthy breast tissue[17] and correlated intracellular influx of sodium with proliferation of brain cancer[18-19]. More recent research has further correlated elevated extracellular sodium concentrations to key events in tumor progression, including upregulation of glycolytic enzymes, DNA damage, inflammation, and metastasis[1].

Specifically, one hallmark of cancer, known as the Warburg Effect, is the metabolic tendency to favor glycolysis over cellular respiration, even in conditions of ample oxygen availability[3,15]. It has been proposed that the Warburg Effect is involved in helping to prepare cancer cells to tolerate hypoxic conditions found in the TME and to meet demands of increased lipid synthesis for cellular division[3]. Epstein et al. reported that the Warburg Effect can arise in

order to meet altered energy demands of active transport systems, and they experimentally induced the Warburg Effect in human cells by increasing extracellular osmotic stress[20]. Because Na^+ plays a major role in both regulating osmotic pressure and mediating a variety of complex cellular transport systems, many of which are disrupted in cancer, this suggests a mechanism by which abnormal sodium concentrations may contribute to the Warburg Effect. Subsequent studies by Amara et al. confirmed this link by directly demonstrating that exposure to hypertonic NaCl culture solutions causes increased lactate fermentation and growth in breast cancer cells[21].

Another important hallmark of cancer influenced by sodium concentration is angiogenesis, the process in which new blood vessels are formed[3,15]. Angiogenesis is instrumental to supplying the growing tumor with nutrients and is promoted by the vascular endothelial growth factor (VEGF) [3,15]. High sodium concentrations are implicated in facilitating angiogenesis by promoting VEGF expression via the nuclear factor of activated T-cells (NFAT5), which is a transcription factor that helps to regulate intracellular tonicity[3,22]. Thus, evidence suggests elevated Na^+ in the TME may be a precursor to the angiogenic processes that promote tumor growth.

Moreover, sodium plays a role in inflammation and influences immune cell activity[3]. Specifically, high sodium concentrations increase the prevalence of tumor-associated macrophages, M2, which exacerbate cancer progression[3,23]. Sodium also affects $CD4^+$ T cell differentiation in ways that support tumor progression and metastasis[3]. Therefore, elevated sodium concentration is both directly and indirectly related to a variety of pro-tumorigenic processes, implicating it as an important cancer biomarker. As such, measuring TME sodium concentration *in vivo* could provide valuable insight into cancer progression and treatment response. The ultimate goal of this research would be to enable precision medicine approaches

whereby patient xenograft tumors could be imaged in murine models to better inform diagnosis and treatment options[12].

2. Sodium Sensing

Applications for quantitative measurement of ions, such as sodium, span a diverse range of fields, each with their own unique set of criteria[5]. For biomedical imaging, an ideal sodium sensing system should be able to quantitatively and inexpensively measure sodium concentrations *in vivo* with high sensitivity, high 3D spatial resolution, minimal invasiveness, and low toxicity. Despite the variety of sodium sensing methods reported in the literature, these criteria have not been sufficiently addressed by a single technique[1]. For example, ^{23}Na-MRI is a method developed specifically for biomedical applications of sodium sensing that has been applied to brain imaging in clinical studies of Alzheimer's[24], multiple sclerosis[25-26], and cancer[27]. However, despite the advantage of offering non-invasive measurements of sodium concentration, ^{23}Na-MRI cannot be performed with standard MRI machines, but rather requires specialized, expensive equipment inaccessible to most researchers and healthcare providers[1]. Furthermore, ^{23}Na-MRI has limited spatial resolution. For example, in the aforementioned clinical studies, the highest resolution of the reported scans was of voxel size 1 mm^3 by Petracca et al.[26] (whose protocol also included scans of voxel size 5 x 5 x 5 mm^3 and 8 x 8 x 10 mm^3) while Paling et al.[25] utilized scans of voxel size 1 mm^3, 1 x 1 x 2 mm^3, 1 x 1 x 4 mm^3, and 4 x 4 x 4 mm^3, and Mohamed et al.[24] reports a resolution of voxel size 4 x 4 x 4 mm^3. In addition to the poor resolution, high cost, and associated limited availability, conventional ^{23}Na-MRI suffers from long acquisition times that prevent real-time monitoring and an inability to distinguish

extracellular from intracellular sodium concentrations, confounding the contribution of phenomena unique to each compartment[1,25-26].

Conversely, sensing methods originating from the field of analytical chemistry are not readily transferable to *in vivo* applications. Inductively coupled plasma mass spectrometry[28], flame atomic absorption spectroscopy[29], ion chromatography[30], and other techniques common in food science and environmental chemistry[31], require extensive sample preparation protocols that are only suitable for biological analysis *ex vivo*. Electrochemical sensors, including potentiometric sensors, voltametric sensors, and electrochemical biosensors, require direct contact between the detector and the sample, resulting in invasive insertion of electrodes into the tissue[5,32]. Although miniaturized electrochemical sensors[32] and microelectrodes[33-34] have been developed and applied to living models, they remain invasive and have limited spatial resolution that requires complex multielectrode arrays[5,35].

Further advances in this field led to the development of ion-selective optodes which link ion recognition to an optical readout to enable contactless signal detection[5]. Miniaturization of such optodes to the nanoscale produces nanosensors that are less invasive, less expensive, and less toxic than their electrochemical counterparts[5,10]. Other advantages of nano-optodes are that they are reversible, enable spatially resolved ion measurements, can selectively localize to tumor tissue due to the enhanced permeability and retention effect, and can be appended with targeting moieties for further tissue specificity[5,36,38,45].

Ionophore-based optical sensors (IBOS) are a class of optodes that employ ionophores, or hydrophobic species that bind specific analytes with high affinity[5]. Sodium Ionophore X (NaIX) is a popular ionophore among sodium-sensitive IBOS due to its high sodium selectivity[6-11]. In IBOS with non-chromogenic ionophores, such as NaIX, binding of the ion to the ionophore is

indirectly coupled with a change in optical properties of a separate, chromogenic dye[1, 6-11]. The majority of ionophore-based sodium nanosensors in the literature operate on a proton-exchange mechanism by which the introduction of the positively charged sodium ion into a hydrophobic nanosensor core alters the protonation state of a pH indicator dye (chromoionophore)[5-11]. Despite the predominance of such a proton-exchange mechanism, it renders the nanosensors cross-sensitive to pH. This pH cross-sensitivity is problematic for *in vivo* applications because acidic pHs, such as those encountered in the TME[15], can result in false positive measurements.

One notable exception to the standard proton-exchange mechanism is a nanosensor developed by Kaur & Kaur that uses a Biginelli ligand as a chromogenic ionophore for sodium ions[2]. However, their highest reported sodium measurement of 40 µM Na^+ is substantially smaller than serum or extracellular concentrations (~135 mM – 145 mM Na^+)[2]. Consequently, the proposed biological applications of their sensor are currently limited to *ex vivo* analysis where the samples can be diluted prior to measurement[2]. The solvatochromic-dye-based nanosensor for potassium ion detection reported by Xie et al. represents another innovative sensing scheme that eliminates pH dependency[37]. Their nanosensor utilized a solvatochromic dye, whose optical properties depend on the hydrophobicity of the environment rather than on protonation state, so as to detect K^+. This research presented here builds upon the work of Xie et al.[37] to develop a solvatochromic-dye based Na^+ nanosensor. In addition to achieving high selectivity and pH independence, the following paper presents, to the author's knowledge, the first quantitative demonstration of biocompatibility and the first photoacoustic application of an IBOS sodium nanosensor.

III.   Methodology

Materials. Unless otherwise specified, all reagents were purchased from Sigma-Aldrich. Two exceptions include polystyrene-graft-poly(ethylene oxide) (PS-g-PEO), which was purchased from Polymer Inc and SD2, which was synthesized in the Kopelman Lab using the following previously reported procedure[37-38]. Solvatochromic Dye II (SD2) was synthesized by dissolving 1.5 g 2-methylbenzothiazole and 3.8 g 1-iodooctadecane in acetonitrile and refluxing for 24 hours. Once cooled, diethyl ether was added to the mixture to precipitate the crude product. Several diethyl ether washes were performed on the collected product before combining 265 mg of the precipitate with 122 mg (dimethylamino)cinnamaldehyde in acetic anhydride and refluxing for 20 minutes. A warm 10 mM sodium iodide solution was combined with the refluxed mixture to yield SD2 (dark purple precipitate), which was then isolated.

Preparation of SD NaNP. To synthesize one batch of the nanosensor, methanol stock solutions of the needed reagents were first prepared as follows: 10 mg/mL PS-g-PEO, 1 mg/mL Solvatochromic Dye II (SD2), 1 mg/mL Sodium Ionophore X (NaIX), and 1 mg/mL sodium tetrakis[3,5-bis(trifluoromethyl)phenyl]borate (NaTFPB). From these stock solutions, 5 mg PS-g-PEO, 0.2 mg SD2, 1.07 mg NaIX, and 0.9 mg NaTFPB were combined in a scintillation vial. 1 mL of the solution mixture was injected into 40 mL of Millipore water while stirring under compressed air at upwards of 700 rpm for at least 30 minutes. The nanosensor solution was then concentrated via centrifuge filtration to 1.5 mL (~5 mg/mL). For samples taken in pH-buffered solutions, after the water was filtered out, the nanosensor was resuspended in and washed with the respective buffer before being brought to the final 1.5 mL volume.

Response Calibrations. All absorbance spectra were collected by UV-Visible (UV-Vis) spectroscopy using a Shimadzu 2600 UV-Vis Spectrophotometer at the University of Michigan.

UV-Vis measurements were taken on 1 mL samples containing 0.5 mg/mL SD NaNP in the appropriate solution. To make these samples, stock salt solutions were freshly prepared via serial dilution and pipetted into the cuvettes to achieve the desired concentration (typically, 0.1, 0.3, 1, 3, 10, 30, 100, 300, and 1000 mM Na^+). To mimic physiological conditions of the extracellular fluid[39-41], sodium response calibration data was collected in a pH-buffered "pseudo-blood" solution containing 10 mM 3-(N-Morpholino)propane sulfonic acid (MOPS), 5 mM KCl, 2.5 mM $CaCl_2$, and 1 mM $MgCl_2$ at pH 7.4. Of note, the presence of these additional ions was determined not to interfere with the nanosensor's measurements according to ion selectivity experiments (Figure 3).

Photoacoustic experiments were performed in collaboration with and using equipment from the Xueding Wang Lab at the Michigan Medicine Medical Sciences Building II. The nanosensor was prepared at a concentration of 20 mg/mL in the pseudo-blood buffer and measurements were taken on 100 μL samples at 0, 1, 3, 10, 30, 100, and 300 mM Na^+. Each sample was injected into a transparent PVC tube, which was submerged in water. The photoacoustic system was comprised of a Continuum tunable pulsed laser and Philips CL15-7 128-element ultrasound probe.

For both UV-Vis and photoacoustic calibrations, the absorbance ratio, R, represents the absorbance at 520 nm over the absorbance at 630 nm. These wavelengths were chosen because their ratio produced the largest signal variation. Normalized ratiometric absorbance, R/R0, was calculated by dividing the absorbance ratio, R, at the respective cation concentration, by the absorbance ratio, R0, at 0 mM of that cation.

Selectivity Experiments. For the cation selectivity experiments, the nanosensor was prepared as outlined above, and its UV-Vis absorbance was measured in a pH 7.4 MOPS-

buffered solution (10 mM MOPS) containing the desired concentrations of either NaCl, KCl, CaCl$_2$, MgCl$_2$, LiCl, or (NH$_4$)$_2$SO$_4$, respectively. The pH sensitivity experiments were performed in solutions containing the desired concentration of NaCl, 10 mM MOPS, 5 mM KCl, 2.5 mM CaCl$_2$, and 1 mM MgCl$_2$ titrated to the respective pH (5.4, 6.4, 7.4, or 8.4) with NH$_4$OH. Notably, it was determined by selectivity experiments that these non-sodium analytes do not affect the nanosensor's readout (Figure 3).

Stability Assay. A double batch of the SD NaNP reaction mixture was prepared by combining 1.8 mg NaTFPB, 0.4 mg SD2, 10 mg PS-g-PEO, and 2.14 mg NaIX from methanol stocks. 2 mL of this reaction mixture was injected into each of two round bottoms containing 80 mL of Millipore water. After stirring under compressed air for at least 30 minutes, the two solutions were separately concentrated via centrifuge filtration. One batch was brought to a final volume of 3 mL (~5 mg/mL) in Millipore water. The other batch was resuspended in 20 mL of pseudo-blood buffer before being centrifuged back down to a final concentration of 3 mL (~5 mg/mL). Both batches were stored at room temperature in a covered box with limited light exposure. On days 0, 2, 4, and 7 following the nanosensor's synthesis, UV-Vis absorbance spectroscopy measurements were taken of the SD NaNP in 0, 0.1, 1, 10, 100, and 1000 mM Na$^+$ in the same solution as the nanosensor was stored (either Millipore water or pseudo-blood buffer, respectively). On each day, the samples were prepared by combining 100 μL of the SD NaNP solution, 500 μL of the respective sodium stock solution, and 400 μL of either pseudo-blood buffer or Millipore water in a 1mL cuvette. For consistency, all sodium stock solutions were freshly prepared via serial dilution each day.

Toxicity Assays. MTT toxicity assays were conducted on a 96-well plate containing 0.1 mL of Hela cells in media. For each of the following treatment groups, 8 trial wells were

prepared containing: 1 mg/mL SD NaNP, 0.1 mg/mL SD NaNP, 0.05 mg/mL SD NaNP, Buffer, PS-g-PEO (0.7 mg/mL), SD2 (0.028 mg/mL), Millipore water (Control), or a solution of methanol and water that was blown under compressed air (Methanol Control). For the treatment groups containing SD NaNP, the nanosensor was synthesized according to the protocol described above and concentrated to a volume of 750 µL (~10 mg/mL) in Millipore water via centrifuge filtration. 250 µL of this solution was diluted with 2.25 mL of Millipore water to obtain a 1 mg/mL nanosensor solution. A 0.5 mg/mL nanosensor solution was made by combining equal parts (1 mL) Millipore water and 1 mg/mL nanosensor solution. 11 µL of these solutions were added to 0.1 mL treatment wells to yield final SD NaNP concentrations of 1 mg/mL, 0.1 mg/mL, and 0.05 mg/mL, respectively.

Solutions of free PS-g-PEO and of free SD2 were also prepared at concentrations equal to the expected concentration of these components in the 10 mg/mL SD NaNP solution (7 mg/mL PS-g-PEO and 0.28 mg/mL SD2). This was accomplished by adding 350 µL of a 10 mg/mL PS-g-PEO methanol stock solution into 0.5 mL of Millipore water in a scintillation vial and 140 µL of a 1 mg/mL SD2 methanol stock solution into 0.5 mL of Millipore water in another scintillation vial. Both these solutions were blown under compressed air for at least 30 minutes so as to evaporate off the methanol. As a metric for the toxicity of any lingering methanol, a Methanol Control was prepared by injecting 350 µL of pure methanol into 0.5 mL of Millipore water and letting it sit under compressed air for the same amount of time. The Control Treatment received a solution of pure Millipore water. A Buffer Treatment was also prepared using the pseudo-blood buffer solution (10 mM MOPS, 5 mM KCl, 2.5 mM $CaCl_2$, & 1 mM $MgCl_2$ at pH 7.4).

11 µL of the respective treatment solution was added to each well, which contained 100 µL of Hela cells in growth media. There was also a row of 8 wells containing only growth media to allow noise from absorbance by the growth media itself to be taken into account. Following a 24-hour incubation, (3-(4,5-dimethylthiazol-2-yl)-2,5-diphenyltetrazolium bromide (MTT) was added, and the cells were incubated for another 4 hours. The MTT crystals were then solubilized with DMSO, and UV-Vis measurements were taken using a plate reader. The average absorbance across the 8 trial wells for each treatment group was calculated after subtracting for noise of the growth media and was compared to the Control Treatment so as to obtain cell viability data.

Size Characterization. Size characterization of the SD NaNP was performed using dynamic light scattering (DLS) measurements collected with instruments at the University of Michigan Department of Chemistry technical services. SD NaNP was synthesized according to standard protocol (see above) and added to solutions containing $0 - 1000$ mM Na^+ in Millipore water. Each sample was 100 µL and contained 0.5 mg/mL SD NaNP at the desired sodium concentration. 10 DLS acquisitions were performed per sample.

IV.   Results and Discussion

The solvent displacement method was used to synthesize sodium-sensitive ionophore-based nanosensors, SD NaNP. As with other ionophore-based nanosensors[5], SD NaNP consists of a polymer capsule (PS-g-PEO), an ionophore (NaIX) to bind the analyte of interest, a dye (SD2) whose absorption reports on the analyte concentration, and a counterion (TFPB⁻) to maintain electroneutrality. In the case of SD NaNP, the capsule is made from PS-g-PEO, whose hydrophilic head groups face outwards to form an aqueous layer while the nonpolar tail groups

are sequestered inwards, forming a hydrophobic core. SD2 is likewise amphipathic, consisting

of a hydrophobic tail and a positively charged head group, whose charge is balanced by the

TFPB⁻ counterion. Uniquely, SD NaNP does not require any plasticizing agent, such as DOS, to

facilitate diffusion within the particle. The plasticizer-free nature of SD NaNP offers several key

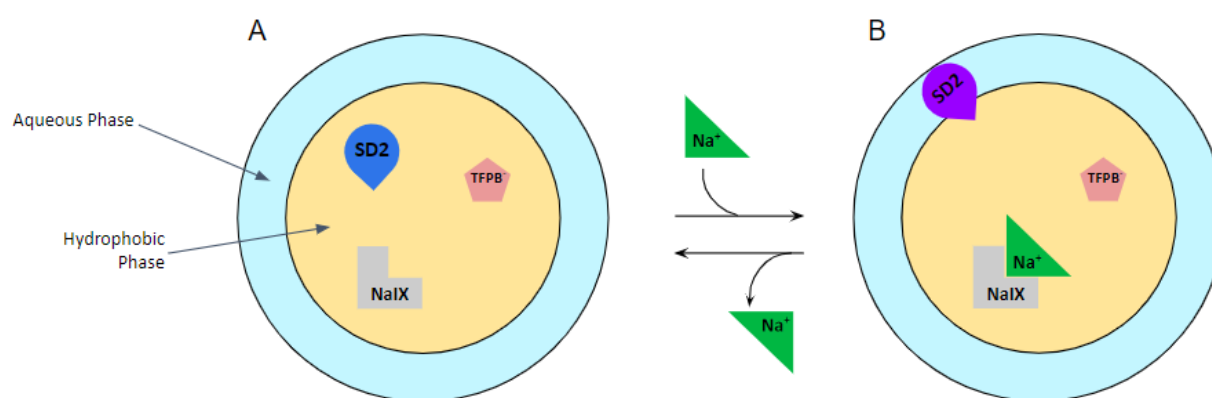advantages over plasticizer-containing nanosensors, including lower toxicity and decreased

manufacturing costs.

Figure 1 – Sensing Mechanism of SD2 NaNP
The PS-g-PEO polymer capsule that forms SD NaNP consists of an aqueous outer layer and hydrophobic core. (A) In the absence of Na⁺, the ionophore [NaIX], counterion [TFPB⁻], and solvatochromic dye [SD2] are embedded within the hydrophobic core. (B) When Na⁺ enters the nanosensor, it binds to NaIX and introduces electrostatic repulsions that push SD2 into the aqueous phase, where it absorbs at a lower wavelength.

The sensor mechanism can be represented by a two-state equilibrium model (Figure 1).

In the absence of sodium (Figure 1A), the sensor components are situated within the

hydrophobic core of the nanosensor, NaIX is unbound, and the positively charged head group of

SD2 is balanced by the TFPB⁻ counterion. When a sodium ion enters the nanosensor, it binds to

NaIX in the hydrophobic core (Figure 1B). The resulting electrostatic repulsions between the

sodium ion and SD2 push SD2 from the hydrophobic core into the aqueous phase at the outskirts

of the nanosensor (Figure 1B). In aqueous environments, SD2 undergoes a blueshift in its

absorbance spectrum. This visually corresponds to a blue-to-purple color change of the sodium

solution (Figure 2B) and can be quantitatively measured via UV-Vis spectroscopy (Figures 2A &

2C). Therefore, the sodium concentration can be correlated to the absorbance of the nanosensor

because, the greater the amount of Na$^+$ present in the solution, the stronger the blueshift of SD2.
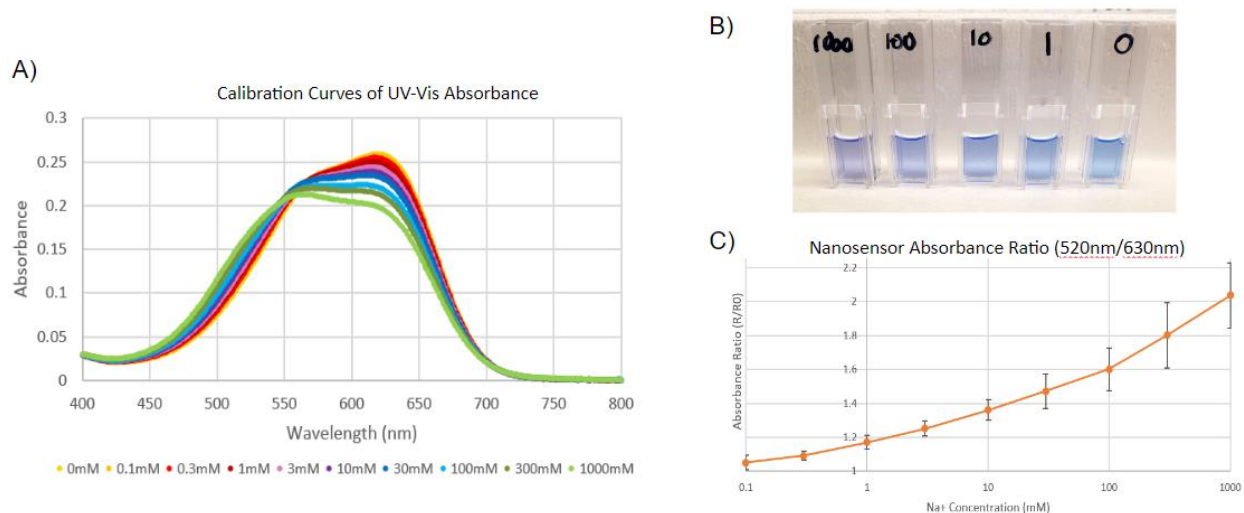

Figure 2 – Absorbance Spectra of SD NaNP
(A) UV-Vis calibration curves of the SD NaNP in pH 7.4 MOPS-buffered pseudo-blood solutions show a decrease in 630 nm absorbance as sodium concentration increases. (B) Image of SD NaNP samples at, from left to right, 1000, 100, 10, 1, and 0 mM Na$^+$ in pH 7.4 MOPS-buffered pseudo-blood salt solutions. (C) Plot of the average normalized absorbance ratio [520 nm / 630 nm] of SD NaNP in pH 7.4 MOPS-buffered pseudo-blood salt solutions. Measurements were taken using UV-Vis spectroscopy, and absorbance was normalized by dividing the absorbance ratio, R, at each Na$^+$ concentration by the absorbance ratio, R0, at 0 mM Na$^+$. Error bars represent one standard deviation in each direction.

The calibration curves of SD NaNP at different Na$^+$ concentrations were collected in both

Millipore water and pH-buffered solutions. The characteristic UV-Vis absorbance spectrum of

SD NaNP is shown in Figure 2A. As sodium concentration increases, SD NaNP exhibits a

decrease in 630 nm absorbance, an increase in 520 nm absorbance, and an isosbestic point at 550

nm. A plot of the ratio of 520 nm absorbance over 630 nm absorbance displays a strong log-

linear increase with sodium concentration (Figure 2C). A ratiometric response, as opposed to

measuring a single wavelength's absorbance, is highly desirable for a nanosensor. First, since

the absorbance of the two wavelengths varies inversely, plotting their quotient increases the

sensitivity of the sensor. Moreover, by internally normalizing the signal, ratiometric

measurements eliminate the signal's dependence on sensor concentration. This is important for

in vivo applications where concentration is difficult to precisely control[8]. Additionally, as

reflected by the small standard deviation, the sensor is highly consistent at low Na^+ concentration

(< 30 mM). As Na^+ concentration increases, signal variation also increases, reflected by the

larger error bars.
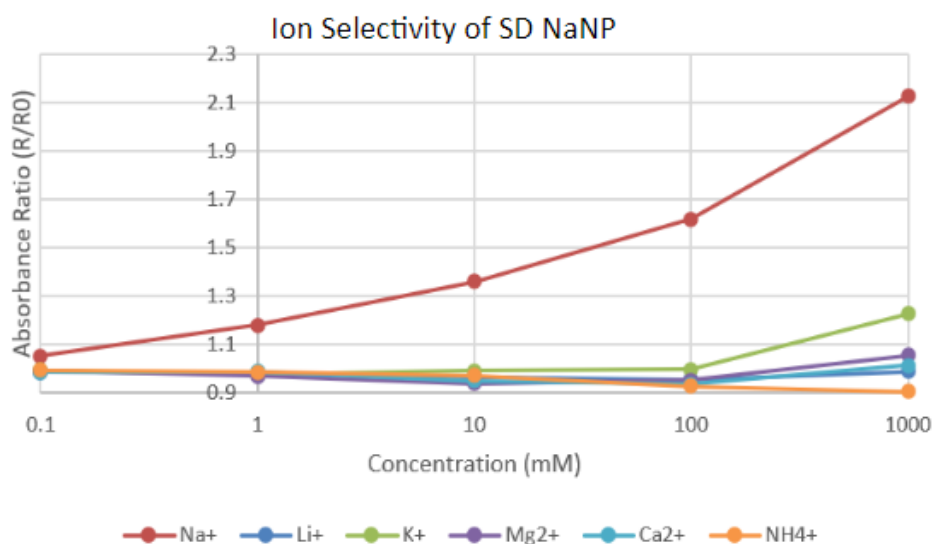
Figure 3 – Ion Selectivity of SD NaNP
Plot of the normalized UV-Vis absorbance ratio (520 nm / 630 nm) of SD NaNP across increasing concentrations of physiologically relevant cations (Na^+, K^+, Li^+, Mg^{2+}, Ca^{2+}, and NH_4^+) shows that only Na^+ causes a substantial change in absorbance ratio. Absorbance was normalized by dividing the absorbance ratio, R, at each cation concentration by the absorbance ratio, R0, at 0 mM of that cation.

In order to test the ability of SD NaNP to discriminate Na^+ from other cations, ion

selectivity experiments were performed (Figure 3). The SD NaNP was exposed to increasing

concentrations of different biologically relevant cations (Na^+, K^+, Li^+, Ca^{2+}, Mg^{2+} and NH_4^+) and

the spectral responses were measured and compared. Consistent with the sodium calibration

results, SD NaNP responded to increasing Na^+ concentrations with a blueshift in peak absorbance, producing a log-linear increase in ratiometric absorbance of 520 nm over 630 nm. In contrast, very little variation in the absorbance spectra was observed for the other cations. As illustrated by Figure 3, the 520 nm over 630 nm absorbance ratio remains relatively constant across 0 – 100 mM for the non-Na^+ species. Notably, there is a slight uptick in the absorbance ratio at 1000 mM K^+, but this is quite small compared to that of Na^+ and well beyond the typical pathophysiological range of K^+ (40 – 50 mM) in the TME[42]. Thus, it should not pose any issue for *in vivo* applications. Therefore, because the nanosensor exhibits little to no response to large concentration changes of other physiologically relevant cations, it can be concluded that SD NaNP is highly selective for Na^+.
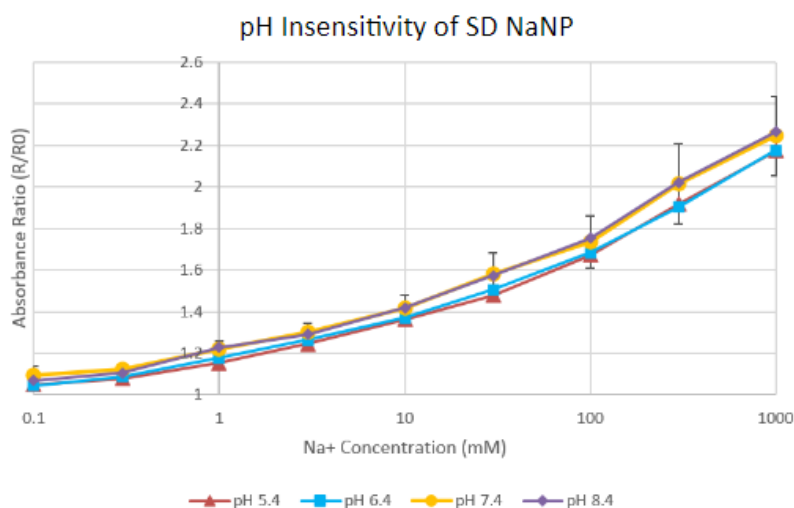

Figure 4 – pH Insensitivity of SD NaNP
Plot of the normalized UV-Vis absorbance ratio (520 nm / 630 nm) of SD NaNP nanosensors in MOPS-buffered salt solutions (10 mM MOPS, 5 mM K^+, 2.5 mM Ca^{2+}, 1 mM Mg^{2+}) at pH 5.4, 6.4, 7.4, and 8.4. Absorbance was normalized by dividing the absorbance ratio, R, for each sample by the absorbance ratio, R0, at 0 mM Na^+ at the corresponding pH. Error bars for the pH 7.4 calibration are provided and represent one standard deviation in each direction.

Additionally, pH sensitivity experiments were conducted to assess how changes in pH influence SD NaNP's response to Na^+ (Figure 4). While physiological pH is considered to be 7.4, TME pH can range from 6.5 to 6.9[36]. As such, it is important that nanosensors remain

insensitive to pH to ensure pH deviations do not confound the measurements. However, most

previously reported sodium nanosensors utilize proton-exchange dyes that result in cross-

sensitivity to pH[5-11]. By employing a solvatochromic dye, SD NaNP was hypothesized to be pH-

independent. In accordance with this hypothesis, strong agreement is observed between the

absorption ratios of the tested pH values of 5.4 – 8.4 (Figure 4), which is well-beyond the

fluctuation ranges that would be encountered for *in vivo* imaging applications. SD NaNP is

therefore pH-independent, providing a major advantage over previously reported sodium
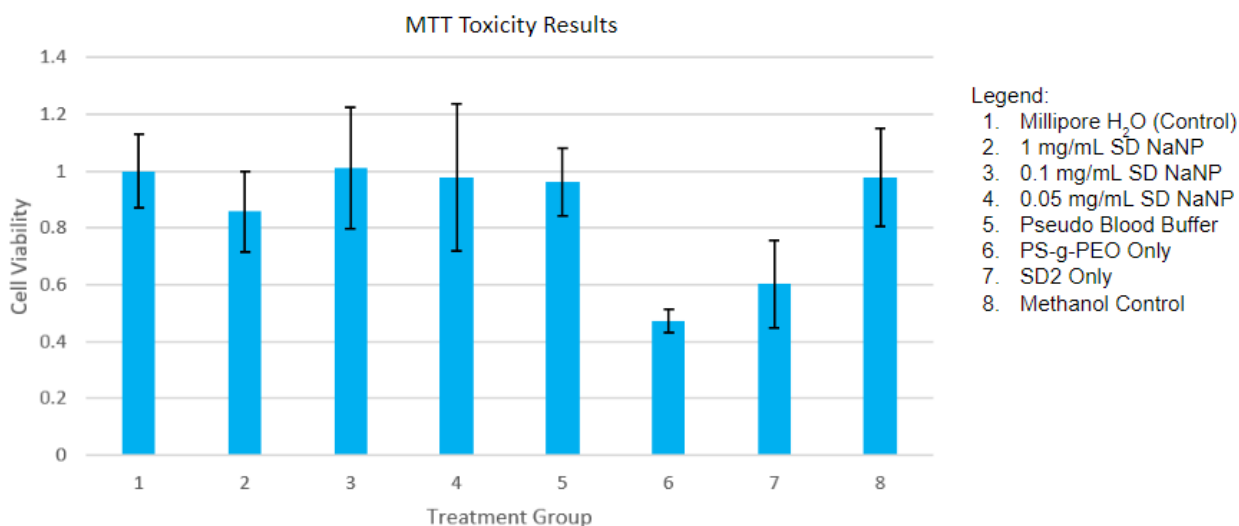
nanosensors.

Figure 5 – Biocompatibility of SD NaNP
Cell viability of Hela cells exposed to (1) Millipore water [Control], (2) 1 mg/mL SD NaNP in Millipore water, (3) 0.1 mg/mL SD NaNP in Millipore water, (4) 0.05 mg/mL SD NaNP in Millipore water, (5) pH 7.4 pseudo-blood solution [10 mM MOPS, 5 mM KCl, 2.5 mM CaCl$_2$, 1 mM MgCl$_2$], (6) 0.7 mg/mL PS-g-PEO, (7) 0.028 mg/mL SD2, and (8) a solution of water and methanol that was blown under compressed air [Methanol Control], as determined by MTT assay. Absorbance data was averaged across the 8 wells from each treatment group, normalized for background noise from the growth media, and compared to that of the Control. Error bars represent one standard deviation in each direction.

In order for nanosensors to be suitable for *in vivo* applications, they must also be

biocompatible so as not to harm the organism. Compared to nanosensors that employ

plasticizers, SD NaNP contains less exogenous compounds, enhancing its biocompatibility.

Additionally, MTT assays were performed to quantitatively assess the toxicity of SD NaNP. In

these experiments, Hela cells were exposed to SD NaNP at three different concentrations (0.05 mg/mL, 0.1 mg/mL, and 1 mg/mL), PS-g-PEO only, SD2 only, pseudo-blood buffer, evaporated methanol in water, or pure Millipore water (Control). Figure 5 depicts the cell viability of each treatment group. As shown, the cell viability of all three SD NaNP treatment groups were very close to, and well within error of, that of the Control (Figure 5). Therefore, it can be concluded that SD NaNP is not toxic to any statistically significant extent at concentrations up to and including 1 mg/mL.

Conversely, the free PS-g-PEO polymer and SD2 dye did exhibit notable toxicity, resulting in lower cell viability than the Control (Figure 5). This toxicity cannot be attributed to residual methanol since the Methanol Control Treatment, which was treated with the same methanol evaporation protocol, did not result in a significant decrease in cell viability (Figure 5). Instead, the higher toxicity of these components compared to SD NaNP may be explained by their lower bioavailability when sequestered in the nanosensor. While the two treatment groups were within error of one another, free PS-g-PEO appears more toxic than free SD2. This heightened toxicity of PS-g-PEO compared to SD2 can likely be attributed to its higher concentration. Specifically, these treatment groups received the same amount of free PS-g-PEO and SD2, respectively, as the expected mass of the corresponding component in the 1 mg/mL nanosensor treatment group. Hence, since PS-g-PEO accounts for a larger percentage of the nanosensor's mass, it was present at a higher concentration than SD2.

Stability of a nanosensor is indicated by the consistency of its response over time. For commercial purposes, good stability is desirable because it enables nanosensors manufactured in one location to be distributed and stored prior to use. To test the effects of storage conditions on the nanosensor's stability, SD NaNP synthesized from the same reaction mixture (see

Methodology) was evenly split between two batches: one suspended in water and the other

suspended in pseudo-blood buffer. UV-Vis spectra were then collected in 0 – 1000 mM Na$^+$

solutions in either Millipore water (Figure 6) or pseudo-blood buffer (Figure 7), respectively, on

days 0, 2, 4, and 7 following the synthesis. Although SD NaNP responded to sodium with an

increase in absorbance ratio on each day, the magnitude of signal change between 0 – 1000 mM

Na$^+$ had decreased by Day 2 for both batches (Figures 6A & 7A). This indicates that SD NaNP

is not stable enough to be stored at room temperature for long periods in water nor buffer

because it lost a sizable degree of sensitivity over the course of 48 hours. Nevertheless, while it

would be more convenient if the nanosensor could be stored for several days after synthesis,

typical *in vivo* protocols[12,38] only require a couple hours or less between nanosensor injection and

measurement. As such, this should not affect the ability of SD NaNP to be applied *in vivo*.
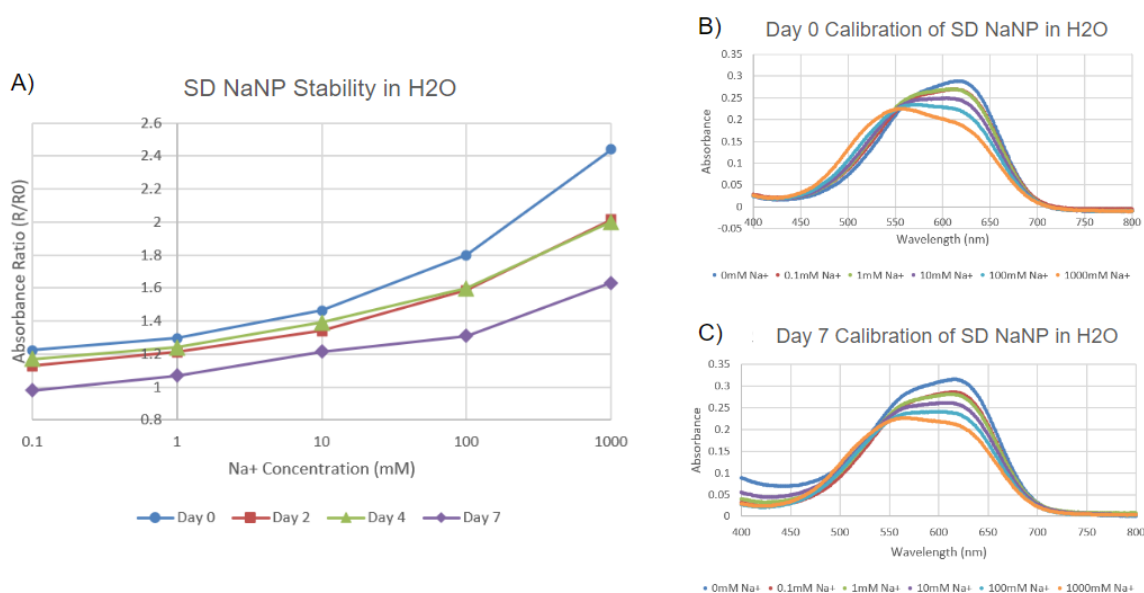

Figure 6 – Stability of SD NaNP Stored in Millipore Water
(A) Plot of the UV-Vis absorbance ratio [520 nm / 630 nm] on Day 0, 2, 4, and 7 following synthesis of SD NaNP nanosensors suspended and stored in Millipore water. Absorbance was normalized by dividing the absorbance ratio, R, for each Na$^+$ concentration by the absorbance ratio, R0, at 0 mM Na$^+$ that day. (B) UV-Vis calibration curves of SD NaNP in Millipore water immediately following its synthesis [Day 0]. (C) UV-Vis calibration curves of SD NaNP in Millipore water seven days after its synthesis [Day 7].
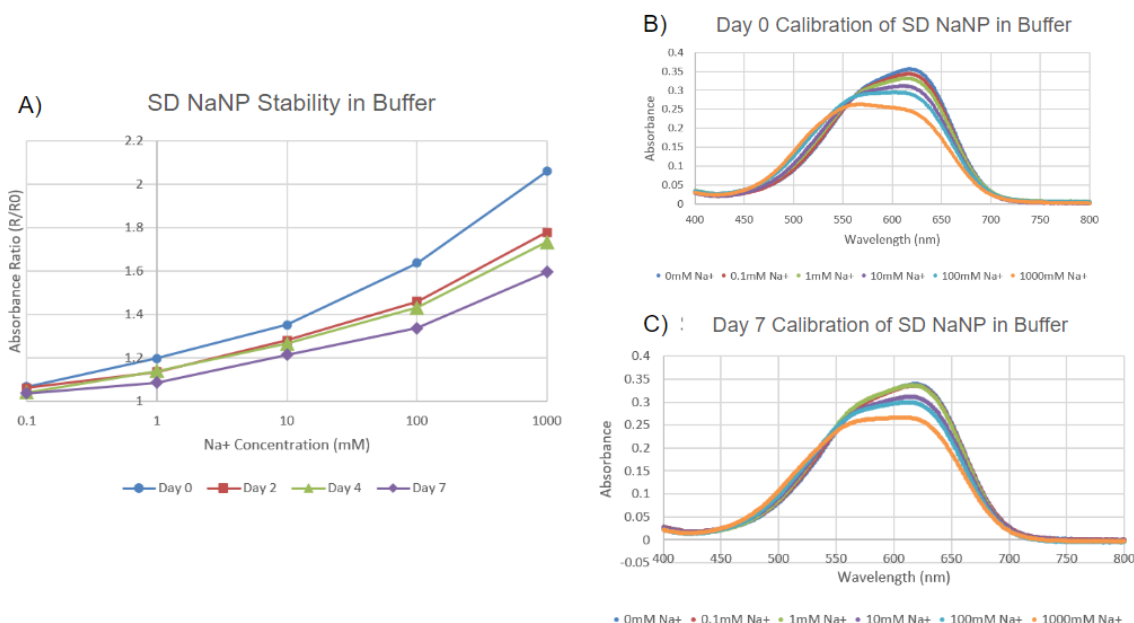
Figure 7 – Stability of SD NaNP Stored in Buffer
(A) Plot of the normalized UV-Vis absorbance ratio [520 nm / 630 nm] on Day 0, 2, 4, and 7 following synthesis of SD NaNP nanosensors suspended and stored in pseudo-blood buffer [10 mM MOPS, 5 mM KCl, 2.5 mM CaCl$_2$, 1 mM MgCl$_2$ at pH 7.4]. Absorbance was normalized by dividing the absorbance ratio, R, for each Na$^+$ concentration by the absorbance ratio, R0, at 0 mM Na$^+$ that day. (B) UV-Vis calibration curves of SD NaNP in pseudo-blood buffer immediately following its synthesis [Day 0]. (C) UV-Vis calibration curves of SD NaNP in pseudo-blood buffer seven days after its synthesis [Day 7].

Over time, the magnitude of signal change continued to decrease for the SD NaNP stored in the pseudo-blood buffer as represented by the decreased slope of the ratiometric absorbance curve (Figure 7A) and subdued change to the 630 nm peak intensity on Day 7 (Figure 7C). In contrast, approximately parallel ratiometric absorbance curves with similar magnitudes of change were observed between Days 2 through 7 for SD NaNP stored in Millipore water (Figure 6A). While the absorbance values at each sodium concentration are somewhat lower by Day 7 for the Millipore water condition (Figure 6A), a prominent decrease in 630 nm peak intensity and increase in 520 nm absorbance similar to that on Day 0 are still observed (Figures 6B & 6C). This suggests that, rather than continuing to lose sensitivity, the SD NaNP stored in Millipore water remained relatively stable between Days 2 through 7. Therefore, storage in Millipore water was more effective than storage in pseudo-blood buffer because the nanosensor

was more stable and lost less sensitivity when stored in water. Informed by these results, future work may be done to optimize the storage conditions of SD NaNP to further enhance long-term stability. Until such time, it is recommended that the nanosensor be used on the same day as it is synthesized for maximum sensitivity.

Notably, the batch suspended in Millipore water showed a larger magnitude of signal variation over the $0 - 1000$ mM Na^+ range on Day 0 (Figure 6A) compared to the buffer-suspended batch (Figure 7A). This finding was quite surprising because, since the batches were prepared from the same reaction mixture, there is not expected to be a difference between the proportions of the sensing components. Moreover, since the nanosensor is pH-independent and extremely insensitive to non-sodium cations at the concentrations present in the pseudo-blood buffer (5 mM K^+, 2.5 mM Ca^{2+}, and 1 mM Mg^{2+}), it is highly unlikely that the difference would be caused by a response to the buffer components. One possible explanation may be that the higher ionic strength of the buffer affects diffusion within the nanosensor, but further investigation would be needed to verify this hypothesis. Either way, the calibrations taken in the pseudo-blood buffer are most reliable for the *in vivo* applications because they most closely mimic physiological conditions of the extracellular fluid.
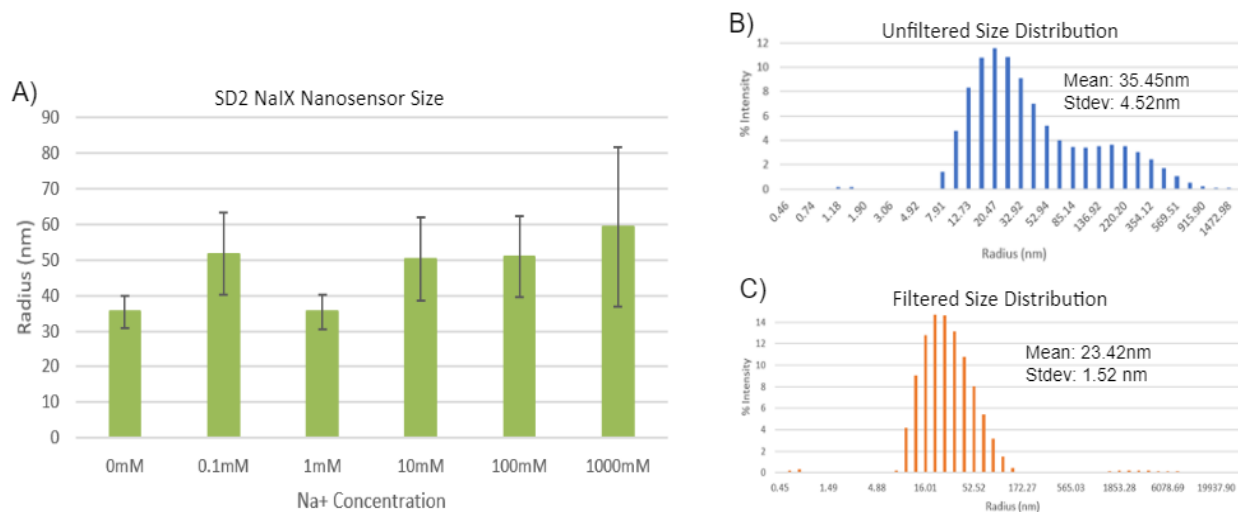
Figure 8 – DLS Size characterization of SD NaNP
(A) Average size of unfiltered SD NaNP by Na^+ concentration, as determined by DLS analysis. Bar height represents the average radius across 10 acquisitions, and error bars represent one standard deviation in each direction. (B) Multimodal size distribution of unfiltered SD NaNP solution at 0 mM Na^+, as determined by DLS analysis. (C) Unimodal size distribution of filtered SD NaNP nanosensor solution at 0 mM Na^+, as determined by DLS analysis.

Another important criteria for nanosensors is size. Access to the tumor from the bloodstream is dependent on the nanosensor's ability to safely pass through the capillaries and diffuse through the endothelial layers to the tumor site[43]. The smaller the nanosensor, the more likely it will be able to pass through these barriers and successfully reach the target tissue[43-44]. Unimodal size distribution and size stability are also desirable because they indicate consistency in the nanosensor size. Size characterization performed on unfiltered samples of SD NaNP in 0 – 1000 mM Na^+ solutions revealed an average particle size of 47.2 nm with an average standard deviation of 9.66 nm (Figure 8A). Measurements for all six samples were within error of one another, with no significant nor consistent trend between size and sodium concentration observed (Figure 8A). Therefore, it can be concluded that the particle size is stable across sodium concentrations of 0 – 1000 mM. While a multimodal distribution was observed at each measured concentration (for example, Figure 8B), syringe filtration, which was subsequently performed on

the 0 mM sample, was successful at obtaining a unimodal size distribution (Figure 8C).

Additionally, the removal of the large particles via the filtering process decreased the average

particle size to just 23.42 nm in radius with a standard deviation of 1.52 nm. Therefore, SD

NaNP that are small, unimodally distributed, and stable in size can be obtained by passing the

nansensor solution through a syringe filter. According to previous research by Tang et al.,

nanosensors of this size achieve optimal tumor retention because they allow for deep tissue
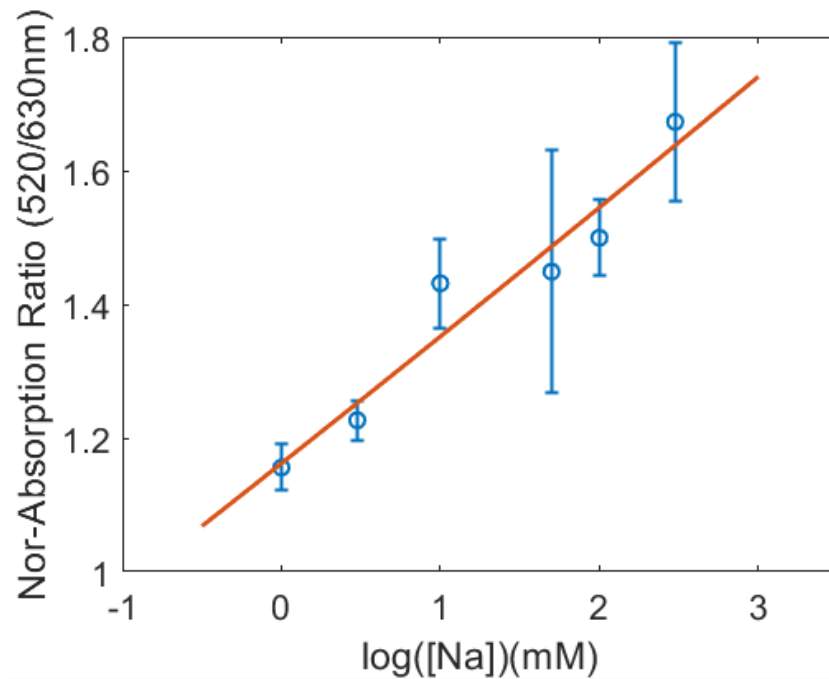
penetration and reduced clearance[44].

Figure 9 – Photoacoustic Calibration of SD NaNP
Normalized photoacoustic absorption ratio (520 nm / 630 nm) of SD NaNP measured *in vitro* at 20 mg/mL in pH 7.4 MOPS-buffered pseudo-blood salt solutions. The photoacoustic absorbance was normalized by dividing the absorbance ratio, R, at each Na^+ concentration by the absorbance ratio, R0, at 0 mM Na^+. Error bars represent one standard deviation in each direction.

After characterizing SD NaNP, *in vitro* photoacoustic experiments were performed

(Figure 9). During photoacoustic studies, an incident laser pulse is absorbed by the nanosensors,

which, upon excitation, experience thermal vibrations that produce ultrasound waves. These

ultrasound waves are detected and used to quantitatively measure the absorbance of the nanosensors, which can be correlated to the amount of sodium present in the solution. Photoacoustic imaging is better suited to *in vivo* applications than optical imaging because it allows for deeper tissue penetration, since ultrasound waves are significantly less prone to tissue scattering[13]. The results of the photoacoustic experiments demonstrate a log-linear signal change of approximately 70% across $0 - 300$ mM Na^+ (Figure 9). Larger error bars, indicating higher signal variability, were observed (Figure 9) compared to the UV-Vis calibrations (Figure 2C). This increased variability is common in photoacoustic studies and may be attributable to the increased noise inherent in ultrasound or to photobleaching of the dye, which was observed during the experiments. Nevertheless, these results demonstrate the capability of SD NaNP to produce a strong, log-linear photoacoustic response to changes in sodium concentration. To the best of the author's knowledge, this is the first successful photoacoustic calibration of a sodium nanosensor to be reported in the literature.

V.   Future Directions

Future work for this research includes further optimizing the sensor and applying it to studies of disease states. As with any sensor, there is opportunity to increase the sensitivity of SD NaNP to Na^+. One method of increasing SD NaNP sensitivity is to utilize a solvatochromic dye that is more hydrophilic so that it enters the aqueous phase more readily in the presence of the analyte. Current work is already underway synthesizing such a dye which will then be applied to the nanosensor with the goal of making it more responsive to Na^+. Additionally, it may be beneficial to tune the absorbance of the dye to a higher wavelength such that both absorption peaks are within the near infrared optical window of approximately $600 - 900$ nm[13].

Though it is of lower priority, future work may also want to focus on determining conditions in which SD NaNP can be stored for prolonged periods without appreciable loss of sodium sensitivity.

Having completed the characterization and *in vitro* photoacoustic imaging experiments, another important next step would be to conduct *in vivo* photoacoustic imaging experiments on xenograft tumors in murine models. Specifically, an investigation of the relationship between extracellular sodium concentration and cancer staging and therapy response could provide insights for timely cancer diagnosis and for informing treatment options to help improve patient outcomes. For this purpose, an active targeting moiety can be attached to the nanosensor, such as a peptide that specifically targets cancer cells[45].

Lastly, SD NaNP could be applied to studying other disease states linked to sodium dysregulation, such as chronic inflammation[3], Alzheimer's disease[24], kidney disease[46], and cardiovascular disease[46]. For the study of excitable cells, such as neurons and cardiomyocytes, future works may also focus on decreasing the response time of the sensor to the order of milliseconds[6] such that brief changes in sodium concentration due to membrane depolarization could be visualized.

VI.   Conclusion

In conclusion, this paper presents a sodium nanosensor, SD NaNP, as a method of ratiometrically quantifying sodium concentrations in *in vivo* applications, such as photoacoustic cancer imaging. The characterization of the nanosensor detailed herein demonstrates that SD NaNP is highly selective, pH-independent, biocompatible, and, on average, only 23.42 nm in radius when filtered. Additional advantages of the SD NaNP nanosensor include that it is

plasticizer-free, thus reducing associated toxicity and manufacturing costs, and it produces a ratiometric response, which controls for the influence of sensor concentration on absolute absorbance. Moreover, *in vitro* photoacoustic experiments demonstrated the ability of SD NaNP to be used for photoacoustic imaging, which allows deeper tissue penetration for *in vivo* medical applications. Future directions for this research include further optimization to improve the nanosensor's sensitivity, stability, and response time, as well as applications of the nanosensor to studies of *in vivo* disease models.

VII.   Acknowledgements

Works Cited

1. Leslie, T. K., James, A. D., Zaccagna, F., Grist., J. T., Deen, S., Kennerley, A., Riemer, F., Kaggie, J. D., Gallagher, F. A., Gilbert, F. J., & Brackenbury, W. J. (2019). Sodium homeostasis in the tumour microenvironment. *BBA - Reviews on Cancer*, *1872*(2), 188304. https://pubmed.ncbi.nlm.nih.gov/31348974/

2. Kaur, G. & Kaur, N. (2018). Estimation of sodium ions using easily engineered organic nanoparticles-based turn-on fluorescent sensor: Application in biological and environmental samples. *Sensors and Actuators D: Chemical, 265,* 134-141. https://doi.org/10.1016/j.snb.2018.02.063

3. Amara, S. & Tiriveedhi, V. (2017). Inflammatory role of high salt level in tumor microenvironment. *Int. Journal of Oncology*, *50*(5), 1477-1481. https://doi.org/10.3892/ijo.2017.3936

4. Lamy, C. M., Sallin, O., Loussert, C., & Chatton, J. Y. (2012). Sodium sensing in neurons with a dendrimer-based nanoprobe. *ACS Nano*, *6*(2), 1176-1187. https://doi.org/10.1021/nn203822t

5. Mistlberger, G., Crespo, G. A., & Bakker, E. (2014). Ionophore-based optical sensors. *Annual Review of Analytical Chemistry*, *7*(1), 483-512. https://doi.org/10.1146/annurev-anchem-071213-020307

6. Dubach, J. M., Das, S., Rosenzweig, A., & Clark, H. A. (2009). Visualizing sodium dynamics in isolated cardiomyocytes using fluorescent nanosensors. *Proc. Natl. Acad. Sci. U. S. A.*, *106* (38), 16145. https://doi.org/10.1073/pnas.0905909106

7. Balaconis, M. K. & Clark, H. A. (2012). Biodegradable optode-based nanosensors for in vivo monitoring. *Anal. Chem.*, *84*(13), 5787-5793. https://doi-org.proxy.lib.umich.edu/10.1021/ac301137c

8. Ruckh, T. T., Mehta, A. A., Dubach, J. M., & Clark, H. A. (2013). Polymer-Free Optode Nanosensors for Dynamic, Reversible, and Ratiometric Sodium Imaging in the Physiological Range. *Sci. Rep.*, *3*, 3366. https://doi.org/10.1038/srep03366

9. Xie, X., Mistlberger, G., & Bakker, E. (2013). Ultrasmall Fluorescent Ion-Exchanging Nanospheres Containing Selective Ionophores. *Anal. Chem., 85*(20), 9932-9938. https://doi.org/10.1021/ac402564m

10. Galyean, A. A., Behr, M. R., & Cash, K. J. (2018). Ionophore-based optical nanosensors incorporating hydrophobic carbon dots and a pH-sensitive quencher dye for sodium detection. *Analyst, 143,* 458-465. https://doi.org/10.1039/C7AN01382E

11. Ferris, M. S., Behr, M. R., & Cash, K. J. (2019). An ionophore-based persistent luminescent 'Glow Sensor' for sodium detection. *RSC Advances*, *9*(56), 32821-32825. https://doi.org/10.1039/c9ra05313a

12. Lee, C. H., Folz, J., Tan, J. W. Y., Jo, J., Wang, X., & Kopelman, R. (2019). Chemical imaging in vivo: Photoacoustic-based 4-dimensional chemical analysis. *Anal. Chem.*, *91*, 2561-2569. https://doi.org/10.1021/acs.analchem.8b04797

13. Beard, P. (2011). Biomedical photoacoustic imaging. *Interface Focus*, *1*(4), 602-631. https://doi.org/10.1098/rsfs.2011.0028

14. D'Alonzo, R. A., Gill, S., Rowshanfarzad, P., Keam, S., MacKinnon, K. M., Cook, A. M., & Ebert, M. A. (2021). In vivo noninvasive preclinical tumor hypoxia imaging methods: a review. *Int. J. Radiat. Biol., 97*(5), 593-631. https://doi.org/10.1080/09553002.2021.1900943.

15. Hanahan, D. & Weinberg, R. A. (2000). The hallmarks of cancer. *Cell*, *100*, 57-70. https://doi.org/10.1016/S0092-8674(00)81683-9

16. Roma-Rodrigues, C., Mendes, R., Baptista, P. V., & Fernandes, A. R. (2019). Targeting tumor microenvironment for cancer therapy. *Int. J. Mol. Sci.*, *20*(4), 840. https://doi.org/10.3390/ijms20040840

17. Sparks, R. L., Pool, T. B., Smith, N. K., & Cameron, I. L. (1983). Effects of amiloride on tumor growth and intracellular element content of tumor cells in vivo. *Cancer Res.*, *43*(1), 73-77.

18. O'Donnell, M. E. & Villereal, M. L. (1982). Membrane potential and sodium flux in neuroblastoma X glioma hybrid cells: Effects of amiloride and serum. *J. Cell. Physiol.*, *113*(3), 405-412. https://doi.org/10.1002/jcp.1041130308

19. O'Donnell, M. E., Cragoe, E. Jr., & Villereal, M. L. (1983). Inhibition of Na^+ influx and DNA synthesis in human fibroblasts and neuroblastoma-glioma hybrid cells by amiloride analogs. *J. Pharmacol. Exp. Ther.*, *226*(2), 368-372.

20. Epstein, T., Xu, L., Gillies, R. J. & Gatenby, R. A. (2014) Separation of metabolic supply and demand: Aerobic glycolysis as a normal physiological response to fluctuating energetic demands in the membrane. *Cancer Metab.*, *2*(7). https://doi.org/10.1186/2049-3002-2-7

21. Amara, S., Zheng, M., & Tiriveedhi, V. (2016). Oleanolic acid inhibits high salt-induced exaggeration of Warburg-like metabolism in breast cancer cells. *Cell Biochem. Biophys.*, *74*, 427-434. https://pubmed.ncbi.nlm.nih.gov/27236294/

22. Amara, S., Alotaibi, D. & Tiriveedhi, V. (2016). NFAT5/STAT3 interaction mediates synergism of high salt with IL-17 towards induction of VEGF-A expression in breast cancer cells. *Oncol. Lett.*, *12*, 933-943. https://pubmed.ncbi.nlm.nih.gov/27446373/

23. Boutilier, A. J. & Elsawa, S. F. (2021). Macrophage polarization states in the tumor microenvironment. *Int. J. Mol. Sci.*, *22*(13), 6995. https://doi.org/10.3390/ijms22136995

24. Mohamed, S. A., Herrmann, K., Adlung, A., Paschke, N., Hausner, L., Frölich, L., Schad, L., Groden, C., & Kerl, H. U. (2021). Evaluation of Sodium (23Na) MR-imaging as a Biomarker and Predictor for Neurodegenerative Changes in Patients With Alzheimer's Disease. *In Vivo*, *35*(1), 429-435. https://doi.org/10.21873/invivo.12275

25. Paling, D., Solanky, B. S., Riemer, F., Tozer, D. J., Wheeler-Kingshott, C. A. M., Kapoor, R., Golay, X., & Miller, D. H. (2013). Sodium accumulation is associated with disability and a progressive course in multiple sclerosis, *Brain*, *136*(7), 2305-2317. https://doi.org/10.1093/brain/awt149

26. Petracca, M., Vancea, R. O., Fleysher, L., Jonkman, L. E., Oesingmann, N., & Inglese, M. (2016). Brain intra- and extracellular sodium concentration in multiple sclerosis: a 7 T MRI study, *Brain*, *139*(3), 795-806. https://doi.org/10.1093/brain/awv386.

27. Poku, L. O., Cheng, Y., Wang, K., & Sun, X. (2021). ^{23}Na-MRI as a noninvasive biomarker for cancer diagnosis and prognosis. *J. Magn. Reson. Imaging*, *53*(4), 995-1014. https://doi.org/10.1002/jmri.27147

28. Wilschefski, S. C., & Baxter, M. R. (2019). Inductively Coupled Plasma Mass Spectrometry: Introduction to Analytical Aspects. *The Clinical Biochemist. Reviews*, *40*(3), 115-133. https://doi.org/10.33176/AACB-19-00024.

29. Bader, N. (2011). Sample preparation for flame atomic absorption spectroscopy: An overview. *Rasayan J. Chem.*, *4*(1) 49-55.

30. Thienpont L. M., Van Nuwenborg J. E., & Stöckl D. (1995). Ion chromatography as potential reference methodology for the determination of total sodium and potassium in human serum. *J. Chromatogr. A.*, *706*(1-2), 443-450. https://doi.org/10.1016/0021-9673(95)00152-d.

31. Traiwatcharanon, P., Siriwatcharapiboon, W., & Wongchoosuk, C. (2020). Electrochemical sodium ion sensor based on silver nanoparticles/graphene oxide nanocomposite for food application. *Chemosensors*, *8*(58). https://doi.org/10.3390/chemosensors8030058.

32. Bakker, E. & Qin, Y. (2006). Electrochemical sensors. *Anal. Chem.*, *78*(12), 3965-3984. https://doi.org/10.1021/ac060637m

33. Gyetvai, G., Nagy, L., Ivaska, A., Hernadi, I., & Nagy, G. (2009). Solid contact micropipette ion selective electrode II: Potassium electrode for SECM and in vivo applications. *Electroanalysis*, *21*(17-18), 1970-1976. https://doi.org/10.1002/elan.200904617

34. Truccolo, W., Donoghue, J. A., Hochberg, L. R., Eskandar, E. N., Madsen, J. R., Anderson, W. S., Brown, E. N., Halgren, E., & Cash, S. S. (2011). Single-neuron dynamics in human focal epilepsy. *Nature Neuroscience*, *14*(5), 635-641. https://doi.org/10.1038/nn.2782

35. Driscoll, N., Rosch, R. E., Murphy, B. B., Ashourvan, A., Vishnubhotla, R., Dickens, O. O., Johnson, A., Davis, K. A., Litt, B., Bassett, D. S., Takano, H., & Vitale, F. (2021). Multimodal in vivo recording using transparent graphene microelectrodes illuminates spatiotemporal seizure dynamics at the microscale. *Communications Biology*, *4*(1), 136. https://doi.org/10.1038/s42003-021-01670-9

36. Fernandes, C., Suares, D., & Yergeri, M. (2018). Tumor microenvironment targeted nanotherapy. *Front. Pharmacol.*, *9*, 1230.

37. Xie, X., Szilagyi, I., Zhai, J., Wang, L., & Bakker, E., (2016). Ion-selective optical nanosensors based on solvatochromic dyes of different lipophilicity: From bulk partitioning to interfacial accumulation. *ACS Sens.*, *1*(5), 516-520. https://doi.org/10.1021/acssensors.6b00006

38. J. W. Y. Tan, J. Folz, R. Kopelman, & X. Wang. (2020). In vivo photoacoustic potassium imaging of the tumor microenvironment. *Biomed. Opt. Express*, *11*(7), 3507-3522. https://doi.org/10.1364/BOE.393370

39. Pohl, H. R., Wheeler, J. S., & Murray, H. E. (2013). Sodium and potassium in health and disease. In: Sigel, A., Sigel, H., & Sigel, R. (eds). Interrelations between essential metal ions and human diseases. *Metal Ions in Life Sciences*, *13*. Springer, Dordrecht. https://doi.org/10.1007/978-94-007-7500-8_2

40. Romani, A. M. P. (2013). Magnesium in health and disease. In: Sigel, A., Sigel, H., & Sigel, R. (eds). Interrelations between essential metal ions and human diseases. *Metal Ions in Life Sciences*, *13*. Springer, Dordrecht. https://doi.org/10.1007/978-94-007-7500-8_3

41. Brini, M., Ottolini, D., Calì, T., & Carafoli, E. (2013). Calcium in health and disease. In: Sigel, A., Sigel, H., & Sigel, R. (eds). Interrelations between essential metal ions and human diseases. *Metal Ions in Life Sciences*, *13*. Springer, Dordrecht. https://doi.org/10.1007/978-94-007-7500-8_4

42. Ong, S. T., Ng, A. S., Ng, X. R., Zhuang, Z., Wong, B. H. S., Prasannan, P., Kok, Y. J., Bi, X., Shim, H., Wulff, H., Chandy, K. G., & Verma, N. K. (2019). Extracellular K^+ dampens T cell functions: Implications for immune suppression in the tumor microenvironment. *Bioelectricity*, *1*(3), 169-179. https://doi.org/10.1089/bioe.2019.0016

43. Ferrari, M. (2010). Frontiers in cancer nanomedicine: Directing mass transport through biological barriers. *Trends in Biotechnology*, *28*(4), 181-188. https://doi.org/10.1016/j.tibtech.2009.12.007

44. Tang, L., Yang, X., Yin, Q., & Cheng, J. (2014). Investigating the optimal size of anticancer nanomedicine. *PNAS*, *111*(43), 15344-15349. https://doi.org/10.1073/pnas.1411499111
45. Winer, I., Wang, S., Lee, Y. E., Fan, W., Gong, Y., Burgos-Ojeda, D., Spahlinger, G., Kopelman, R., & Buckanovich, R. J. (2010). F3-targeted cisplatin-hydrogel nanoparticles as an effective therapeutic that targets both murine and human ovarian tumor endothelial cells in vivo. *Cancer research*, *70*(21), 8674-8683. https://doi.org/10.1158/0008-5472.CAN-10-1917
46. Twardowski, Z. J. (2008). Sodium, hypertension, and an explanation of the lag phenomenon in hemodialysis patients. *Hemodial. Int.*, *12*(4), 412-425. https://doi.org/10.1111/j.1542-4758.2008.00304.x